

# BlueKoi: Combining a Tuna-Inspired Tail and Koi-Inspired Body Bending for Maneuverability

Irene Sha<sup>1</sup>, Daniel B. Quinn<sup>2</sup>, and Radhika Nagpal<sup>1</sup>

**Abstract**—As marine ecosystems face rapid declines, field observations have become essential for better understanding our oceans. Fish-inspired robots are a promising solution, as they are less disruptive than propeller-based approaches in sensitive environments. However, in both fish and fish-inspired robots, there is a trade-off between speed (that favors rigid bodies) and maneuverability (that favors flexible bodies). In this work, we present BlueKoi, an untethered, fish-inspired robotic platform that leverages both a stiff tuna-inspired tail for efficient swimming and a koi-inspired rotating head for maneuvering, reaching speeds of 1.84 body lengths per second and a turn radius of 2.03 body lengths. We experimentally quantify the robot's turn radius under varying conditions and develop a reduced-order model to both understand the turning behavior and inform future design decisions, without needing explicit measurements of hydrodynamic coefficients. Furthermore, we show that our model is not only accurate but also capable of extending simulations to account for future design modifications. By decoupling propulsion and maneuverability, BlueKoi is a scalable and modular platform that enables adaptability for diverse sensing and navigation needs.

## I. INTRODUCTION

Critical marine ecosystems — coral reefs, oyster reefs, kelp forests, to name a few —face rapid declines in these changing climates, making field observations increasingly crucial to understand our oceans [1], [2]. Underwater robot swarms can be a compelling solution to consistent monitoring of such sensitive ecosystems, where the collective nature of the swarm enables widespread and coordinated coverage, as well as scalability and robustness to individual robot limitations. Current systems typically involve teams of Remotely Operated Vehicles (ROVs) or Autonomous Underwater Vehicles (AUVs) [3], where individual vehicles are equipped with many propellers to move in three dimensions. This is well suited for open ocean environments, but the resulting propeller turbulence is both noisy to wildlife and potentially destructive in sensitive ecosystems like coral reefs. Fish-inspired robots and swarms have the potential to monitor reef health and navigate complex environments without being as disruptive. However, the overall success a swarm is dependent on the individual robot's ability to navigate well enough to withstand perturbations, coordinate with others, and avoid colliding with the environment.

Fish are incredibly agile and can navigate through strong currents and complex environments with ease [4]. This has inspired significant studies into fish-inspired robot systems.

\*This work was supported by the Office of Naval Research (ONR Award #N00014-22-1-2616). The authors are with the Department of Mechanical and Aerospace Engineering at Princeton University<sup>1</sup> and the Department of Mechanical and Aerospace Engineering at University of Virginia<sup>2</sup>. Email: is2327@princeton.edu

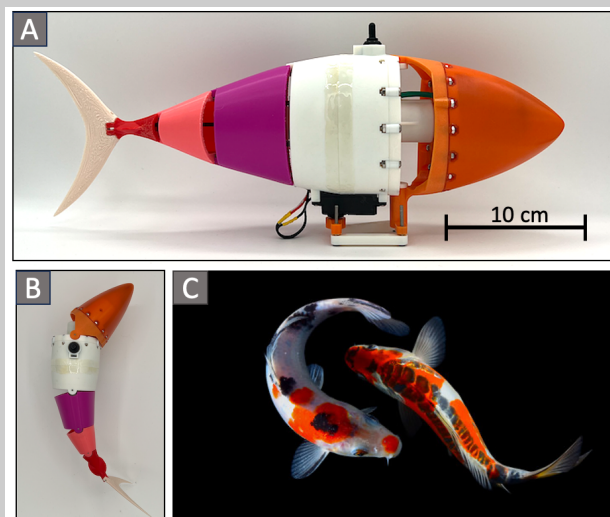


Fig. 1. (A) BlueKoi, an underwater robot inspired by both tuna and koi. (B) Actuated head and maximum amplitude tail, and (C) Koi (*Cyprinus rubrofasciatus* "koi") demonstrating their flexible morphology. Credit: Adobe

Robotic propulsors inspired from fast swimmers such as tuna have made progress in closing the gap between biological and robotic systems, achieving straight-line speeds of 2.02 body lengths per second or BL/s (0.85 m/s) [5], 4.60 BL/s (1.17 m/s) [6], or even 11.6 BL/s (3.7 m/s) [7]. For example, the Tunabot flex [6] is inspired by tuna's streamlined stiff tail and uses a simple design with passive flexible joints to achieve high performance and efficiency. These robotic tails have exciting potential to be deployed in real ocean environments but currently lack the full range of motion needed for autonomous deployment. More complex fish-inspired robots have incorporated varying mechanisms to achieve yaw and depth maneuvers. Mechanisms for yaw (2D turning) include asymmetrical tail flapping, multi-jointed actuated tails, pectoral fins for steering, or a combination of these options [8], [9], [10], [11], [12], [13]. One key example is the SoFi robot, which utilizes an advanced soft tail design for both forward and turning motions, and has been tested in real world coral reef environments [14]. The SoFi robot has a highly complex design using high-precision fabrication techniques, making it difficult and expensive to mass-produce as a swarm. Another key example is the BlueSwarm robot, which uses a multi-fin design with magnetic-coil actuators to maneuver, and has been replicated into a functional underwater swarm [15]. However, compared to fish and even robotic counterparts, their slow and weak swimming and

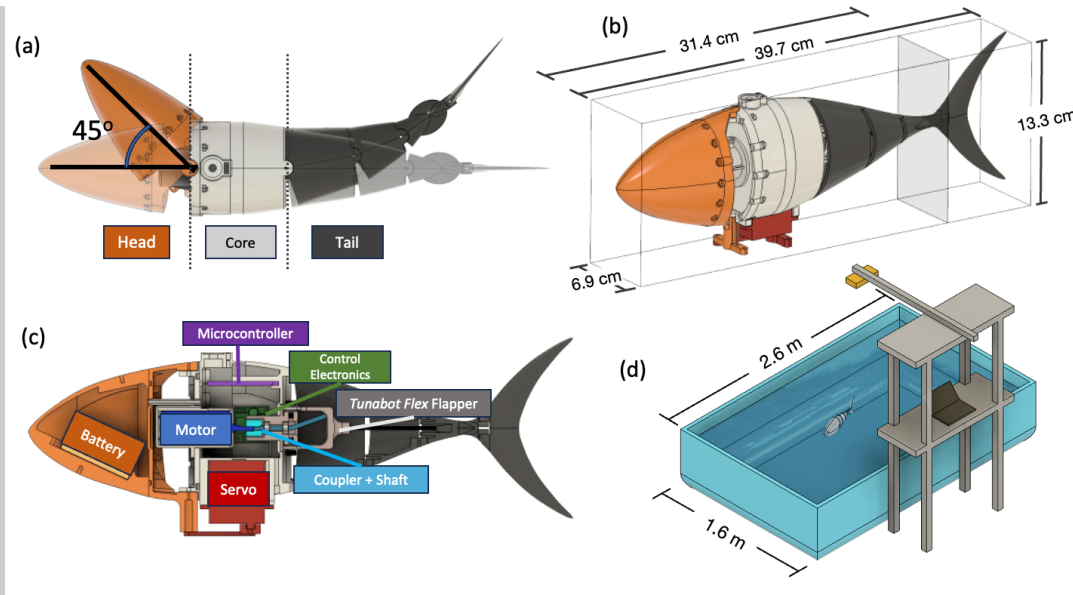


Fig. 2. (A) Full actuation limits of both the head and tail, along with the three main sections. (B) Dimensions of BlueKoi. (C) Internal components of BlueKoi (D) A representation of the experimental setup.

turning make them unsuitable for navigating in real world environments. In addition to the physical design complexity, there is also a lack of computational models that adequately capture the impact of body design choices on resulting navigation abilities. Overall, it remains an open research challenge to design fish-inspired robots that have the ability to achieve high swimming speeds and efficiency like the robotic propulsors [6] but also the necessary maneuverability and design simplicity to create underwater swarms [15].

In this paper, we present the design of a new untethered fish-inspired robot, BlueKoi. Inspired by the koi's bilateral body flexibility and the tuna's high-performance but stiff caudal fin, we achieve 2D maneuvers by integrating a turning "head" that acts as a yaw control surface, combined with an efficient Tunabot Flex tail [6]. This modular design allows the robot to drastically change its overall curvature to turn, while maintaining a highly stiff tail for efficient straight line locomotion. We experimentally quantify the turn radius across a number of critical parameters: motor input power (cruise speed), head angle (body curvature), and head length (body design parameter). Furthermore, we develop a reduced order model that is validated by the experimental data, and that provides insights for future trajectory planning and design changes.

Our contributions extend the state of the art in several ways. BlueKoi investigates a method of maneuvering that is modular enough to combine with pre-existing robotic tails, simple to manufacture, and can be reasonably captured with a data-driven reduced-order model. There is an inherent tradeoff between maneuverability and speed, using only caudal fin, which makes it challenging to design a platform that demands both. A tuna's streamlined but stiff tail allows it to achieve greater maximum swimming speeds but at the cost of its turn radius, compared to other carangiform or

thunniform fish [16]. Our design incorporates not only an efficient and fast tail (based on the Tunabot flex [6]) but also the ability to drastically change its overall curvature despite its overall rigid body. As a result, the BlueKoi robot can mimic some of the benefits that a flexible fish would have by actively controlling the angle of the head [17]. Using this mechanism BlueKoi reaches speeds of 1.84 body lengths per second and a turn radius of 2.03 body lengths. We provide extensive experiments, investigating maneuverability at multiple speeds, as well as the impact of increasing head length. These experiments allow us to validate our reduced-order model and use a data-driven approach to estimating hydrodynamic coefficients. Comparing simulated trajectories to experimental data, the simplified model is highly effective and differs about 10% in the worst case. In summary, by separating the control surface for maneuverability from the control surface for propulsion, the BlueKoi robot demonstrates a modular and maneuverable design, all while being manufactured using 3D printing techniques. Furthermore, the reduced order model can simulate trajectories of unrealized geometric configurations, supporting future design variations that include buoyancy control and camera-based navigation for full autonomy.

## II. ROBOT DESIGN

BlueKoi's overall shape and tail propulsion primarily replicates the Tunabot flex; however, unlike its predecessor, the BlueKoi is fully untethered and contains all control electronics onboard, which required a new design. BlueKoi can be sectioned into three "modules": the tail, the head, and the core (Fig. 2A). Each of these sections can be adjusted to accommodate design needs. The core houses the motor, the servo, and the electronics. The tail is responsible for forwards propulsion, while the head acts as a turning control surface.

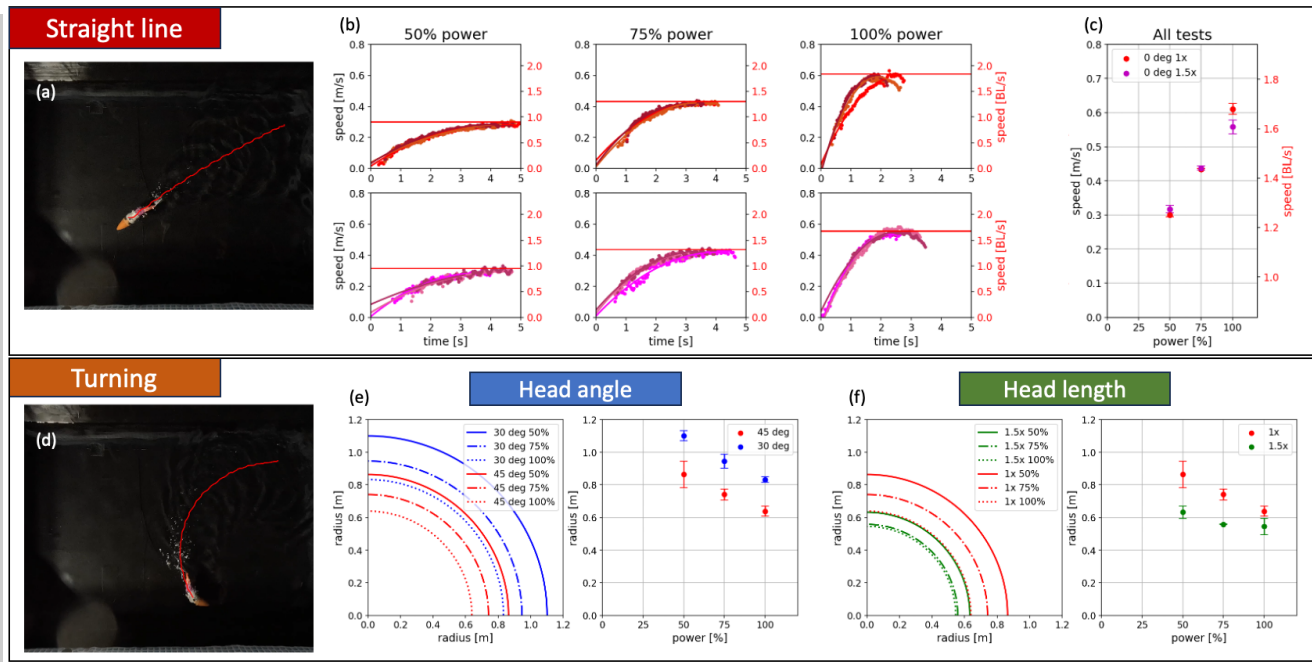


Fig. 3. (A) A snapshot of a straight line experiment. (B) Straight line experimental results; first row represents 1x head length experiments, while the second row represents 1.5x head length. The horizontal line represents the averaged maximum speed. Some data is missing from the beginning of the tests due to occlusion. (C) The average for the tests over the three tested powers, with standard deviations plotted. (D) A snapshot of a turning experiment. (E) Steady state turn radii, while varying head angle, plotted both as a trajectory (left) and as averages with errors (right) (F) Steady state turn radii, while varying head length, plotted both as a trajectory (left) and as averages with errors (right)

To achieve a turn, BlueKoi is equipped with a servo that controls the head's angle with respect to the core, resulting in a curved body shape. This head-turning mechanism is different from approaches that use an actuator to bias the tail joint (e.g. [12]). BlueKoi's active joint position is located in front of the center of mass rather behind it. Thus, the head functions more like a rudder, whereas some other approaches adjust the direction of the flapping propulsor, or use active control to oscillate the joint. Our mechanism is also different from approaches that include an active head joint to steer (e.g. [11]). BlueKoi's mechanisms for maneuverability and propulsion are decoupled, which would make replacing one possible without affecting the other, unlike systems that use all joints to assist in turning. Although in this paper we study a simple case of maneuvering (steering by holding the head constant), our design has the capability to extend into more complex maneuvers, as detailed in Section V.

The overall design is simple to manufacture, using off-the-shelf components and 3D printed body parts. BlueKoi measures 39.7 x 13.3 x 6.9 cm, and weighs 0.72 kg (Fig. 2B), putting it in the same class as other similar robots [7], [12]. For body length (BL) measurements, we use the standard tip to peduncle length (31.4 cm).

#### A. Tail: forwards propulsion

The tail is an underactuated and flexible tail from the Tunabot flex, chosen for its high performance and efficiency. Made of 3D printed PLA, the tail's four joints move passively in response to a flapper that sweeps back and forth in a plane. Despite being made of rigid materials, Tunabot flex reduces

the cost of transport by 53% solely from increased flexibility and reaches speeds of 4.60 BL/s [6]. This is significant in closing the current gap between biological and robotic systems; furthermore, rigid materials are faster and more consistent to manufacture than typical soft materials, simplifying production and making expansion into a swarm easier. For the flapping motion, the motor's rotational movement is converted into the oscillatory motion using a bent shaft in the slot of the flapper, which connected by two arms on a pinned joint. The original paper documents the mechanism in greater detail [6].

Design of the BlueKoi required sizing up the Tunabot flex by 1.5x to include batteries, a servo, onboard electronics, and waterproofing. The motor remains the same size but we chose a lower RPM motor to compensate for the larger torque required to actuate a larger tail. We expect to regain the performance from future motor improvements, and we computationally explore the design impact of higher power in Section V.

#### B. Head: turning control surface

The head houses the battery and small weights for ballasting. The entire section is hinged to the core using a pair of set screws, and connected to the servo via a push-stick. The actuation limits are 45 degrees in either direction. The head shell is 3D printed on a Stratasys J55 in Vero resin. Two external holes allow for the mounting of head caps to extend the length of the head for experiments. The head is waterproofed with an O-ring face seal, which allows a user to open the head for servicing.



### C. Core: electronics

The core acts as a watertight interface between the other two sections and houses all the main electronics. The outer shell is also 3D printed with resin on a Stratasys J55. Inside, a microcontroller (ESP32 Wroom) acts as the central controller, which is connected to other electronics: the motor driver (Adafruit DRV8871), the servo input line, a SD card read/write module, and a potentiometer (Bourns 3382H-1-103), as shown in Fig. 2C. A through-wire runs between the head and core, providing power from the battery. Similarly to the head, the core is waterproofed with an O-ring face seal. The motor (ServoCity 485RPM Econ Gear Motor) is housed in the core, protruding slightly towards the head, while the servo (Savox SW1212SG) is inset underneath.

## III. EXPERIMENTS

In order to test how BlueKoi's actuated head affects its maneuverability, we conducted 66 total experiments to test the effects of motor input power, head angle, and head length on the turn radius. We use turn radius as a metric of maneuverability; a smaller radius is beneficial for navigating complex environments. We are not only interested in knowing the minimum radii turn possible, but also how cruising speed (input power) and chosen head angle combine to generate the effective turn radii for future trajectory predictions. The robot directly controls motor input power and the head angle, while head length is explored as a potential design factor for future iterations. Understanding the impact of head length is crucial if the design needs to accommodate new payloads or cameras. The experimental scenarios allow a deeper understanding of the BlueKoi performance and provide data for model simulations (Section IV).

### A. Methods

The robot is placed in a 2.6 m x 1.6 m pool with a water depth of 0.3 m (Fig. 2D). A GoPRO11 mounted above the surface of the water records at 30 frames per second. We use a meter stick to calibrate the video pixels to a real world length. Offline tracking is achieved using DeepLabCut [18]; the snout, head joint, core center, and peduncle are tracked as four separate points. Velocity is derived from differentiating positional data of the core center, as it oscillates the least compared to the other tracked parts, averaged over a moving window of 5 frames. During the experiments, the robot broadcasts an HTTP interface over WiFi, allowing the experimenter to modify motor power, servo angle, and experimental run time. The angular position of the motor shaft is recorded every 5 ms with the potentiometer, which is used to calculate flapping frequency. Due to the size of the pool, there are limitations on the length of the experiment, as the robot may collide with the side of the pool before a full turn is completed.

Three trials were completed for each set of experimental parameters, and their averaged maximum velocities or turn radii are used to construct our data-driven model, described in Section IV. All experiments start at from rest, and all three variables are set to a constant (power, head angle, head

length). Power is changed by varying the PWM input to the motor given by the motor controller, head angle is controlled by the servo angle, and head length is modified by securing a "head cap" on the front of the robot. The unmodified head length is designated as 1x head length in this paper, and adding a head cap that is 1.5x larger is designated as the 1.5x head length. The robot is buoyant at rest but may sink slightly during the course of a trial due to the direction of propulsion. Depending on the maneuver, the robot moves between 3-8 seconds, limited by the pool size.

### B. Results: Straight-line swimming

We conducted straight line swimming experiments to (1), verify that the robot functions correctly with an actively actuated head held at 0 degrees, and (2) quantify the power-speed relationship, even as we change the size of the head.

The averaged maximum speed in the 1x case is 0.61 m/s or 1.84 BL/s; in the 1.5x case, 0.56 m/s or 1.68 BL/s. In all experiments over both 1x and 1.5x head length (Fig 3A), increasing power similarly increases the measured maximum velocity. Furthermore, increasing the head length does not appear to significantly change the overall maximum velocity. This suggests that increasing head length from 1x to 1.5x has a negligible impact on the maximum achievable speed during straight line motion at 50% and 75% power; in 100% power, the longer head reaches a slightly slower maximum speed.

### C. Results: Turning

Fish turn using their flexible bodies to modify their morphology, controlling the fluid forces through both spatial and temporal asymmetry. BlueKoi primarily uses spatial asymmetry of the body, such as actuating the servo that controls the head angle, to achieve a steady turn. In Fig. 3, the experimental turn radius is plotted as a circular trajectory to visualize the different turn radii and also as a scatter plot of the overall averages alongside the standard deviations.

**Head Angle.** The head angle is varied in two tests over three powers: 30 degrees and 45 degrees, the latter being the furthest allowable configuration. Across both head angle configurations, the turn radius decreases with increased input power (Fig. 3D). This suggests that (1) a more angled head angle decreases the turn radius, and (2) a faster swimming speed decreases the turn radius irregardless of the head angle.

**Head Length.** To vary head length, we attach a 3D printed PLA "cap" that effectively increases the head length, and thus, the head's profile area. To combat a change in attitude, we insert a small mass (15 g) to keep the robot level. By increasing the head length, BlueKoi generally achieves a smaller turn radius shown in Fig. 3E, although in the 1.5x case, the decrease in turn radius between 75% power and 100% is less significant.

### D. Analysis

The decrease in turn radius in all cases can be generally attributed to increasing drag on the head, causing an asymmetric force to impart a yaw moment. Increasing the speed (via motor input power) and increasing the profile area

(via larger head angle or larger head length) both increase the drag force. However, increasing the drag on the body decreases the overall speed and efficiency during a turn.

Overall, these experiments prove that BlueKoi is capable of variable turn radii by changing the motor input power and head angle. Even with a longer head, the straight line speed is comparable to the base length and the turn radius is smaller, making this platform versatile in its design.

#### IV. MODEL

Modeling the behavior of BlueKoi is essential for three key reasons: (1) understanding how changing the power and head angles impacts the turn radius, (2) modifying physical parameters such as head length to support future design iterations, and (3) enabling more precise control for trajectory planning. A hydrodynamic model allows us to predict how design changes will impact performance, making it a crucial tool for both refinement and deployment in real-world applications.

BlueKoi achieves turning primarily through unequal lateral forces. As the thrust force can be approximated in the body's forwards direction, actuating the servo causes the head to enter the water flow at an angle. This generates hydrodynamic forces that create a yaw moment, akin to a boat's rudder. However, capturing the exact fluid dynamics involved presents significant challenges due to the complexity of the flow. The robot's morphology and multiple joints makes it difficult to derive exact force equations and coefficients without direct flow channel measurements. This process is time-consuming and brittle across design changes, such as custom head length to fit more internal electronics.

We investigated if a simple hydrodynamic model as a system of two flat plates could capture the basic turning dynamics of BlueKoi. Our model integrates experimental data to determine key parameters that produce simulated trajectories closest to the experimental results, and we evaluate the accuracy of the model by comparing the differences. Then, we use extended simulations to explore a larger design space, such as the effects of a more powerful motor, a wider range of head angles, or a longer head.

##### A. Equations of Motion

In the model, we represent the head as one flat plate (the head plate), and the core plus the tail as another flat plate (the tail plate). These two plates are at an angle represented by  $\phi$ , also known as the head angle (Fig. 4). The *center of mass* acts as the origin of the body coordinates, with the  $x$  axis aligned with the head plate's direction.

We modeled the tail force as a frequency-dependent thrust ( $\mathbf{T}$ ) acting through the BlueKoi's *center of mass*, and we modeled the head as a flat plate entering a flow at some angle of attack  $\alpha$ . As a result, the entire body experiences lift ( $\mathbf{L}$ ), drag ( $\mathbf{D}$ ), and a yaw moment ( $\mathbf{M}$ ) at its *aerodynamic center*, which is located at the quarter chord along the full body length [19]. We prescribe lift and drag inline and perpendicular respectively to the direction of flow; this can be done by a rotation in the complex plane. We can map the

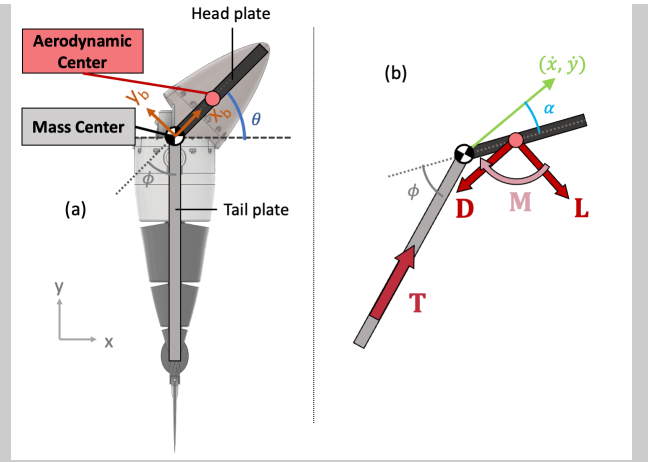


Fig. 4. (A) The model of the robot as two flat plates, with the center of body coordinates inline with the head plate. (B) The forces and moments acting on the body, along with the angle of attack ( $\alpha$ ) and the body velocity  $(\dot{x}, \dot{y})$ , the latter also representing the direction of flow that determines the directions of lift and drag.

rotation in the complex plane back into the body plane by decomposing the resulting vector into its real and imaginary parts.

The force and moments are derived from hydrofoil theory [19] and are represented as:

$$\mathbf{T} = C_T \left( \frac{1}{2} \rho A f^2 \right) (\cos(\phi) e^{i\theta} + \sin(\phi) e^{i(\theta + \frac{\pi}{2})}) \quad (1)$$

$$\mathbf{L} = C_L \left( \frac{1}{2} \rho A \|\dot{x}, \dot{y}\|^2 \right) \frac{\dot{x} + i\dot{y}}{\|\dot{x}, \dot{y}\|^2} (i) \quad (2)$$

$$\mathbf{D} = C_D \left( \frac{1}{2} \rho A \|\dot{x}, \dot{y}\|^2 \right) \frac{\dot{x} + i\dot{y}}{\|\dot{x}, \dot{y}\|^2} (-1) \quad (3)$$

$$\mathbf{M} = C_M \left( \frac{1}{2} \rho A \|\dot{x}, \dot{y}\|^2 \right) - C_{Md} (\dot{\theta} |\dot{\theta}|) \quad (4)$$

The coefficients are defined as:

$$C_L = C_{L\alpha} \sin(2\alpha) \quad (5)$$

$$C_D = C_{D0} + C_{D\alpha} (1 - \cos(2\alpha)) \quad (6)$$

$$C_M = C_{M\alpha} (\sin(2\alpha)) \quad (7)$$

$C_T$  and  $C_{Md}$  are unaffected by the angle of attack due to their relation to the tail geometry and rotational damping.

The state space representation of the equations of motion is defined as:

$$S = \frac{d}{dt} \begin{bmatrix} x \\ y \\ \theta \\ \dot{x} \\ \dot{y} \\ \dot{\theta} \end{bmatrix} = \begin{bmatrix} \dot{x} \\ \dot{y} \\ \dot{\theta} \\ m^{-1} \text{Re}(\mathbf{L} + \mathbf{D} + \mathbf{T}) \\ m^{-1} \text{Im}(\mathbf{L} + \mathbf{D} + \mathbf{T}) \\ I^{-1}(\mathbf{M} + Nl) \end{bmatrix} \quad (8)$$

where  $N$  represents the force perpendicular to the direction of the head plate, and  $l$  represents the distance between

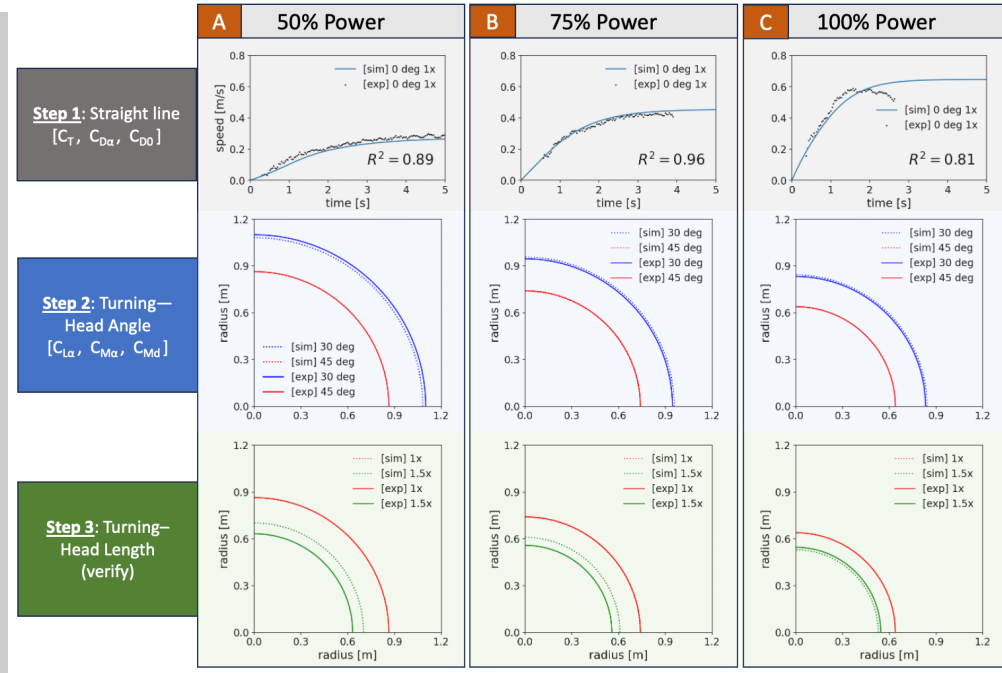


Fig. 5. The three steps taken to tune sets of parameters to match the simulated data (dashed lines) to the experimental data (solid lines). Each of the different powers (A: 50%, B: 75%, and C: 100%) are separately tuned.

the center of mass the aerodynamic center along the head plate. By integrating the forces and moments over time steps to obtain the states, we recover the trajectory of the simulation.

## B. Coefficients

For flat plates in a fluid, we approximate the relationship between angle of attack ( $\alpha$ ) and the sub-coefficients as a constant multiplied by a periodic function. As induced drag ( $C_{D\alpha}$ ) should at a maximum when the plate is perpendicular to the flow, we prescribe the periodicity to be always positive and maximum when  $\alpha = 90^\circ$  and minimum when  $\alpha = 0^\circ$ . We prescribe lift ( $C_{L\alpha}$ ) and moment ( $C_{M\alpha}$ ) to be at a maximum when  $\alpha = 45^\circ$  due to the flat plate simplification.

We chose the coefficient of thrust ( $C_T$ ) to be a constant, representing some scaling as part of the thrust force equation, which itself varies with frequency. Profile drag ( $C_{D0}$ ) is also considered some constant throughout the simulation, as the geometry does not change.

To promote convergence in our simulations, we introduced the damping yaw torque, represented by the coefficient of damping moment ( $C_{Md}$ ). Physically, this term represents the resistance to rotation that submerged bodies feel when they rotate in a fluid. As is typical with damping terms, we imposed the damping torque in the direction opposite of the yaw rotation, and we gave it a magnitude proportional to the yaw rotation speed squared [20].

## V. SIMULATIONS

The goal of our reduced order model is to provide an approximation of the behavior of the robot. For this reason, we are especially interested if our model can predict the

general trends that we observe in the experimental trials. Instead of explicitly measuring the coefficients that determine the hydrodynamic forces, which would be time consuming, we use the data to tune the coefficients in steps, based on the experiment type. We then validate the estimated model with data that was not used in the tuning process. We show that the data-driven model is able to match trends with reasonable accuracy and we further use the model to explore the design space beyond our hardware implementation.

### A. Coefficient Estimation

To estimate the coefficients, we complete the following steps for each of the three tested input powers:

**Step 1) Straight line motion:** [ $C_T$ ,  $C_{D\alpha}$ ,  $C_{D0}$ ]. In straight line swimming, the trajectory is determined by only thrust ( $C_T$ ) and drag ( $C_{D\alpha}$ ,  $C_{D0}$ ). The relationship between these parameters is determined by comparing simulated and experimental velocity data.

When the thrust force equals the drag force, the robot will reach a constant speed. Thus, the relationship between  $C_T$  and  $C_{D0}$  determines the speed at equilibrium, according to Eq. 1 and Eq. 3. Since  $\alpha = 0^\circ$  at initial conditions, and there are no external lateral forces or moments, the angle of attack remains at 0 for the straight line swimming, and the robot does not turn. Therefore, we can fit a value for  $C_T$  for all input powers by simultaneously best matching the approximate equilibrium speed for the 50% power, 75% power, and 100% power, such that we keep  $C_{D0}$  equal to the same constant. This is also inline with our assumptions for the skin friction coefficient  $C_{D0}$ ; since the geometry is not changing, we assume that  $C_{D0}$  remains the same regardless of the maximum velocity. The coefficient  $C_{D\alpha}$  determines

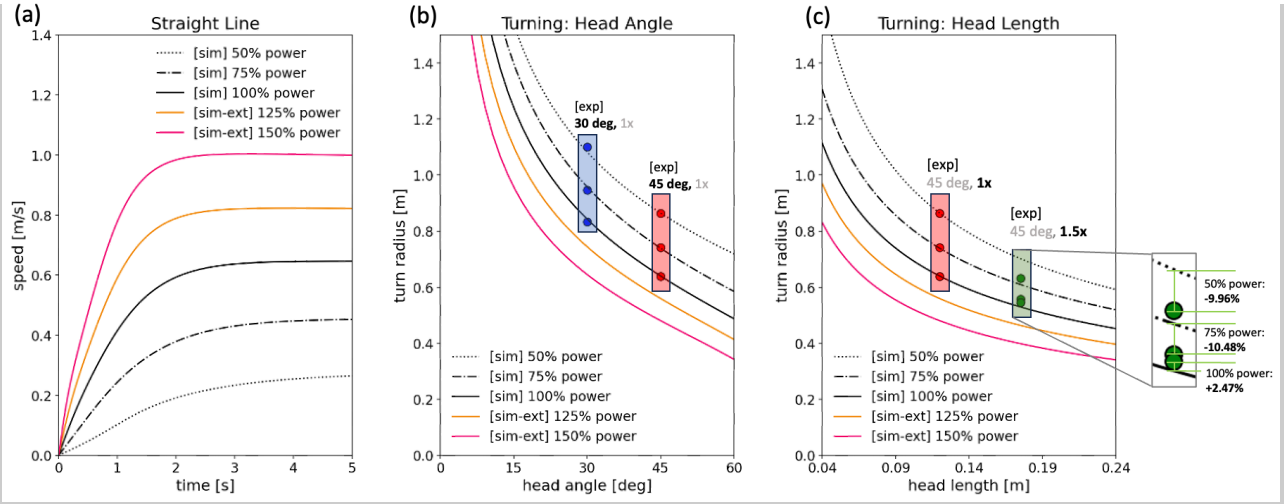


Fig. 6. Simulation results based on the flat-plate model for the tested input powers (50%, 75%, and 100% power), along with extended input powers (125% and 150% power). (A) Simulated straight line speeds for the tested powers. (B) Simulated turn radii across varying head angles. The experimental data is plotted at 30 and 45 degrees. (C) Simulated turn radii across varying head lengths. The experimental data is plotted at 0.12 m (1x head) and 0.175 m (1.5x head). The insert shows the distance between the experimental values and the simulated values for 1.5x head length.

how quickly the maximum speed is reached. We tune the value by minimizing the coefficient of determination  $R^2$  between the simulated values and the experimental values for each separate input power.

**Step 2) Turning motion:  $[C_{L\alpha}, C_{M\alpha}, C_{Md}]$ .** To determine the remaining coefficients, we compare the simulated turn radius with the experimental turn radius. For this step, it is possible to use either the head angle or head length data; we choose to use head angle due to more consistent experimental data. The trajectory, as determined by a particular set of coefficients, is matched to  $\phi = 45^\circ$  and 1x head length within 1% difference, then best matched to  $\phi = 30^\circ$  within 5% difference (see Table II). An exact match of both experimental turn radii to the simulated ones is not guaranteed due to model limitation and experimental noise. We chose to keep  $C_{L\alpha}$  and  $C_{M\alpha}$  a constant; these parameters should remain equal across the trials since they should not change. Thus, we primarily change  $C_{Md}$  across the different power inputs to vary the simulated turn radii.

**Step 3) Turning motion: coefficient verification.** To validate the selected parameters for a given input power, we compare the head length simulation to the corresponding experiments—in particular, we compare the 1.5x length experiment to simulation as a proxy for the accuracy of the model, since there is no direct tuning for this step. The coefficients used in the simulations are shown in Table I.

Although we start with six unknown fluid coefficients, only three require manual tuning, simplifying the process of using experimental data to drive the model.

## B. Data-to-Model Results

The differences between the data and model are listed in Table II. In the 50% power and 75% power cases, the model varies by about 10%; the 100% power case performs the best out of all three. This may be because lower speeds

TABLE I  
TABLE OF FREQUENCY AND COEFFICIENTS

	f (Hz)	$C_T$	$C_{D\alpha}$	$C_{D0}$	$C_{L\alpha}$	$C_M$	$C_{Md}$
50% power	2.37	4.5	0.3	0.5	3.14	0.1	145
75% power	4.02	4.5	2.5	0.5	3.14	0.1	130
100% power	5.82	4.5	4	0.5	3.14	0.1	104

TABLE II  
TABLE OF MODEL-DATA % DIFFERENCES

	50% power	75% power	100% power
% diff (30 deg, 1x)	2.77%	-2.09%	-1.70%
% diff (45 deg, 1.5x)	-9.96%	-10.48%	2.47%

are generally less consistently captured in the experiments (see Fig. 3), which may be caused by fluid motion within the pool. The model is also limited in its accuracy because it makes simplifications about the geometry and does not account for more complex interactions between the water and the robot, such as flow separation at certain angles of attack. Nevertheless, the results demonstrate that the model sufficiently captures the trend in changing head length and head angle.

## C. Design Exploration

For the three varied experimental parameters—input power, head angle, and head length—we extended the simulation beyond what was physically implemented to explore a wider design space. Fig. 6A shows the speed for straight line simulations, and Fig. 6B and C show the simulated turn radii through a range of head angles and head lengths respectively. Because we do not have experimental tests for the extended input powers, we determine the coefficients using linear extrapolation on frequency,  $C_{Md}$ , and  $C_{D\alpha}$ .



**Input power:** Each of the lines in all subplots represent different power input settings, three of the experimentally tested powers (50%, 75%, 100%), and two extended input powers (125% and 150%) that were not physically implemented. In Fig. 6A, we observe that with the extrapolated coefficients, the extended input powers yield proportionally increasing steady state speeds. This allows us to understand how a faster or more powerful motor could change the trajectory of the robot. In the case of turning (Fig. 6B and C), we observe that increasing the input power will decrease the turn radius, as shown by the simulated lines. Moving faster through the water will increase the drag on the head, and thus, decrease the turn radius.

**Head angle and head length:** Based on the simulated turn radii in Fig. 6B and C, we can conclude that increasing head angle and head length will decrease the turn radii. Greater head angles appear to have diminishing returns on the turn radius, which implies that changing the design to accommodate a larger head actuation limit would not yield a much greater turn radius. For the head length, a similar trend is seen: increasing the head length from 0.04 m to 0.14 m yields a greater decrease in turn radius than 0.14 m to 0.24 m. This means that we can expect to see similar turning performance at a set head angle of 45° even if the head length increases. These results suggest the model is capable of describing general trends in changing the head angle and the head length, especially that increasing both decreases the steady state turn radius.

## VI. CONCLUSIONS

In this paper, we demonstrated and experimentally quantified the design of BlueKoi, which combines a tuna-inspired tail for propulsive performance with a koi-inspired body for maneuverability. BlueKoi's straight line swimming speed reached a maximum of 0.61 m/s (1.84 BL/s) at 100% power, and achieved a minimum steady state turn radius of 0.64 m (2.03 BL). Using a low-order model, we captured turning behavior in simulations without extensive fluid coefficient measurements with an accuracy of about 10%. Our experiments and model not only predicted turn radius but also support future design refinements.

There are numerous opportunities for future maneuverability studies using BlueKoi. We can directly explore more complex maneuvers such as underpowered turns, which could enable finer maneuvers without propulsion and be captured by the same low-order model. Additionally, investigating temporal asymmetry in the flapping motion of the tail, alongside an actuated head, may lead to tighter turn radii or faster turns. For autonomous navigation, we can extend the equations of motion to trajectory planning through an obstacle field using control strategies like Rapidly-exploring Random Trees (RRT).

Our reduced-order model is a an effective tool to explore design modifications for full autonomy. For example, we can investigate head length changes to accommodate cameras and vision-processing. For diving, we can also modify the model to incorporate pectoral fins as additional flat plates. Overall,

these advancements move us closer towards a maneuverable and manufacturable fish-inspired robots for field studies.

## ACKNOWLEDGMENT

We thank Joe Zhu and Carl H. White (UVA) for their immense help in replicating the Tunabot flex tail.

## REFERENCES

- [1] J. M. Pandolfi, R. H. Bradbury, E. Sala, T. P. Hughes, K. A. Bjorndal, R. G. Cooke, D. McArdle, L. McClenachan, M. J. Newman, G. Paredes *et al.*, "Global trajectories of the long-term decline of coral reef ecosystems," *Science*, vol. 301, no. 5635, pp. 955–958, 2003.
- [2] N. E. Leonard, D. A. Paley, F. Lekien, R. Sepulchre, D. M. Fratantoni, and R. E. Davis, "Collective motion, sensor networks, and ocean sampling," *Proceedings of the IEEE*, vol. 95, no. 1, pp. 48–74, 2007.
- [3] R. Bogue, "Underwater robots: a review of technologies and applications," *Industrial Robot: An International Journal*, vol. 42, no. 3, pp. 186–191, 2015.
- [4] B. E. Flammang and G. V. Lauder, "Pectoral fins aid in navigation of a complex environment by bluegill sunfish under sensory deprivation conditions," *Journal of Experimental Biology*, vol. 216, no. 16, pp. 3084–3089, 2013.
- [5] S. C. Van Den Berg, R. B. Scharff, Z. Rusák, and J. Wu, "Openfish: Biomimetic design of a soft robotic fish for high speed locomotion," *HardwareX*, vol. 12, p. e00320, 2022.
- [6] C. H. White, G. V. Lauder, and H. Bart-Smith, "Tunabot flex: A tuna-inspired robot with body flexibility improves high-performance swimming," *Bioinspiration & Biomimetics*, vol. 16, no. 2, p. 026019, 2021.
- [7] R. J. Clapham and H. Hu, "isplash: Realizing fast carangiform swimming to outperform a real fish," *Robot fish: bio-inspired fishlike underwater robots*, pp. 193–218, 2015.
- [8] K. Hirata, T. Takimoto, and K. Tamura, "Study on turning performance of a fish robot," in *First International Symposium on Aqua Bio-Mechanisms*. Mitaka, 2000, pp. 287–292.
- [9] X. Chen, J. Yu, Z. Wu, Y. Meng, and S. Kong, "Toward a maneuverable miniature robotic fish equipped with a novel magnetic actuator system," *IEEE Transactions on Systems, Man, and Cybernetics: Systems*, vol. 50, no. 7, pp. 2327–2337, 2018.
- [10] Y. Zhong, Z. Li, and R. Du, "Robot fish with two-dof pectoral fins and a wire-driven caudal fin," *Advanced robotics*, vol. 32, no. 1, pp. 25–36, 2018.
- [11] R. Tong, Z. Wu, D. Chen, J. Wang, S. Du, M. Tan, and J. Yu, "Design and optimization of an untethered high-performance robotic tuna," *IEEE/ASME Transactions on mechatronics*, vol. 27, no. 5, pp. 4132–4142, 2022.
- [12] S. Du, Z. Wu, J. Wang, S. Qi, and J. Yu, "Design and control of a two-motor-actuated tuna-inspired robot system," *IEEE Transactions on Systems, Man, and Cybernetics: Systems*, vol. 51, no. 8, pp. 4670–4680, 2019.
- [13] T. J. Ng, N. Chen, and F. Zhang, "Snapp: An agile robotic fish with 3-d maneuverability for open water swim," *IEEE Robotics and Automation Letters*, 2023.
- [14] R. K. Katschmann, J. DelPreto, R. MacCurdy, and D. Rus, "Exploration of underwater life with an acoustically controlled soft robotic fish," *Science Robotics*, vol. 3, no. 16, p. eaar3449, 2018.
- [15] F. Berlinger, M. Gauci, and R. Nagpal, "Implicit coordination for 3d underwater collective behaviors in a fish-inspired robot swarm," *Science Robotics*, vol. 6, no. 50, p. eabd8668, 2021.
- [16] P. W. Webb, "The biology of fish swimming," *Mechanics and physiology of animal swimming*, vol. 4562, 1994.
- [17] D. Quinn and G. Lauder, "Tunable stiffness in fish robotics: mechanisms and advantages," *Bioinspiration & Biomimetics*, vol. 17, no. 1, p. 011002, 2021.
- [18] A. Mathis, P. Mamidanna, K. M. Cury, T. Abe, V. N. Murthy, M. W. Mathis, and M. Bethge, "Deeplabcut: markerless pose estimation of user-defined body parts with deep learning," *Nature neuroscience*, vol. 21, no. 9, pp. 1281–1289, 2018.
- [19] J. Anderson, *EBOOK: Fundamentals of Aerodynamics (SI units)*. McGraw hill, 2011.
- [20] T. L. Hedrick, B. Cheng, and X. Deng, "Wingbeat time and the scaling of passive rotational damping in flapping flight," *Science*, vol. 324, no. 5924, pp. 252–255, 2009.